PERGAMON

Solid-State Electronics 46 (2002) 1315–1324

SOLID-STATE ELECTRONICS

www.elsevier.com/locate/sse

Enhanced modelization of ion implant simulation in compound semiconductors

J.M. Hernández-Mangas *, L. Enriquez, J. Arias, M. Jaraíz, L. Bailón

Departamento de Electricidad y Electrónica, Universidad de Valladolid, E-47011 Valladolid, Spain

Received 3 September 2001; received in revised form 19 December 2001; accepted 22 January 2002

Abstract

An efficient binary collision approximation ion implant code with enhanced prediction capabilities is presented. It includes recent improvements in physical models for compound semiconductors. It uses only one fitting parameter for low dose implantations. A periodic ab initio full bond electron density for the target is used. Damage accumulation is supported using a modified Kinchin–Pease model. To speed-up the code a refined algorithm for statistical noise reduction is also included in a three-dimensional case, including the lateral and shallow zones. The agreement with experiments is good for different target materials. A comparison with experimental SIMS results for several projectiles and targets is presented.

Keywords: Ion implantation; Binary collision approximation simulation; GaAs; SiC

1. Introduction

Ion implantation is one of the main processes used for the fabrication of modern integrated microelectronic devices. In some semiconductors (e.g. SiC) is the main way to dope it. The new materials are of great importance in the development of fast and powerful electronic devices. The reliable prediction of dopant concentrations by simulations is of great importance in order to save the cost and time required by experiments, even more in the compound materials world.

Knowledge of the three-dimensional (3D) profile of the implanted ions is crucial for current deep sub-micron devices, as this distribution is closely related to the desired electrical characteristics of the final device. The ability to accurately predict the lateral doping profiles as well as the depth profiles in a computationally efficient manner is important for optimum design and fabrication of advanced devices. Also dopant profiles implanted with high energies are needed to create retrograde wells. Channelling of projectiles into the target must be taken into account with physical models, because some projectiles present a strong channelling component [1–4].

To be predictive for different materials and projectiles, a simulation code must be able to simulate different implant conditions like angle, orientation, oxide layer, dose, etc., with the same set of adjustable parameters and models.

Also, the ion implant simulator must allow a trade-off between speed and accuracy [5]. All of these aspects have been studied by different groups and are now scattered across different simulation codes. In a effort to analyze the prediction capabilities and computational efficiency that can be attained with these models, we have gathered them all into a single simulation code. The purpose of this paper is, therefore, to first describe the models implemented and then present an analysis of the performance of the combined use of these models in terms of prediction capabilities and computational efficiency. One conclusion is that we selected the binary collision approximation (BCA) in order to achieve this. The molecular dynamics (MD) technique is more accurate than

* Corresponding author. Tel.: +34-983-423000; fax: +34-983-423675.

E-mail address: jesman@ele.uva.es (J.M. Hernández-Mangas).

0038-1101/02/$ - see front matter
PII: S0038-1101(02)00072-2

BCA, but it needs much longer calculation times. BCA methods can be refined to improve their accuracy to meet the needs.

Historically, researchers have used several modelization schemes to solve the problem of ion implantation. The choice depends on material's characteristics such as amorphous [6] or crystalline [7] targets, and also on the description level of the problem: MD, BCA, transport equation, etc.

Our starting point has been the MARLOWE scheme [7]. It has been completely written in C++ [8–10]. A physical model with only one adjustable parameter has been used [11] for the electronic stopping using a novel integration method. Also to speed-up the simulator a new statistical noise reduction scheme has been implemented.

2. Physical models

Projectiles are simulated following their complete trajectory as well as the trajectories of the recoils generated (full cascade development). The target material is modelled as crystalline, polycrystalline or amorphous [7]. For polycrystalline targets a random rotation of the whole crystal is made before each ion implant. For amorphous, a random rotation of the crystal is done before each collision.

Thermal vibrations are considered using a Debye temperature model [12,13]. Projectiles loose their energy both elastically and inelastically by collisions with the atoms of the target material. The BCA, used here, considers only the collision with one target atom at a time. Simultaneous collisions are modelled through a combination of individual collisions [14] when needed (i.e. channelling conditions).

2.1. Elastic losses: specific screening functions

The nuclear interaction between the incident projectile and the target atom is solved by classical mechanics [15]. A numerical integration of the movement equations for both particles is done. To speed-up the implant simulation, a look-up table is previously calculated. A repulsive Coulombic screened potential is used. By default a universal screening function due to ZBL [6] is used.

We use specific screening functions, when available, for each projectile–target combination obtained by ab initio methods [6] (e.g. with DMol code [16]) to reduce the number of approximations used by the simulator. When no specific screening function is available the best suited seems to be the ZBL one. It has a mean error of 2.1% with respect to specific ones [6].

2.2. Inelastic losses: physical models

It has been found necessary [11] to include energy loss due to inelastic collisions (*local*), and energy loss due to electronic stopping (*non-local*) as two distinct mechanisms in order to obtain good simulation results under a range of channelling conditions [17–19]. It is not possible to assume that one of these processes is dominant and *fit* it to accurately model energy losses for different implant energies and directions.

The non-local inelastic stopping accounts for the average energy loss of the ion as it travels along the interstitial volume of the target. It is due to the interaction between the nucleus of the projectile and the target's electrons. This electronic stopping is given by the modified Brandt–Kitagawa [20] theory with only one adjustable parameter [4,21], r_s^0. This stopping is calculated as

$$S_{\text{non--local}} = \int_{\text{trajectory}} [Z_1^*(v, r_s^0)]^2 S_p(v, r_s)\,\mathrm{d}x \tag{1}$$

where Z_1^* represents the effective charge of the ion [20]; S_p, the electronic stopping power for a proton and $r_s = (3/(4\pi\rho))^{1/3}$, the one-electron radius (ρ is the local electron density). The r_s^0 value is related to the effective electron density of the target and depends on the ion–target combination [4].

The proton stopping depends on the local electron density that results from the crystalline structure of the target. For low energies, a numerical approximation to the model of Echenique et al. [22] is used. For high energies Bethe's model [23] is used.

For the electron density we use a 3D electron charge distribution calculated by the ab initio pseudo-potential total energy method in the local density approximation [24] that includes the true bonds, or the isolate atom density superposition (IADS) approach (see below).

The local inelastic energy loss stopping is related with the close collisions and take into account the electron–electron interaction between the projectile and target atoms. It is described by the modified Firsov theory [25,26] as proposed by Cai et al. [4]:

$$\Delta E_i = \int_{\text{trajectory}} F_{ij}\,\mathrm{d}r \tag{2}$$

where F_{ij} is the repulsive force between projectile and target due to the electron–electron interaction.

As mentioned by Firsov [26], at sufficiently high ion velocities the electrons of the two atoms will not have the time necessary for free interaction, and so the transfer of energy will diminish. We have accounted for this fact by damping out [27] the energy transfer beyond a critical velocity ($v_c = 0.7v_B$, where v_B is the Bohr velocity), as shown below:

$$\Delta E_i^* = \Delta E_i \begin{cases} v/v_B & \text{for } v < v_c \\ v_c^2/(vv_B) & \text{for } v \geqslant v_c \end{cases} \quad (3)$$

In order to obtain a smooth transition between the lower and upper velocity regions, a transfer function [28] is used:

$$f(v) = \frac{2\exp\left(-(v/v_c)^2\right)}{1+\exp\left(-2(v/v_c)^2\right)} \quad (4)$$

2.3. Three-dimensional electron density distribution

The local electron density distribution is used for the calculation of the non-local inelastic stopping. It is very important to tie ends periodicity to reduce the inaccuracies.

The ZBL electron density is a spherically symmetric electron distribution calculated by Ziegler et al. [6] and was used by several authors [4,29,30]. It has a uniform interstitial distribution that does not represent the density of the open channels accurately (see Fig. 1).

The 3D electron density used by us is obtained by means of the ab initio pseudo-potential total energy method in the local density approximation [24]. This is a full description of the covalent bonds of the target material.

When we do not have a full bond description of the electron density (as occurs with compound materials) we use a 3D electron density that we call IADS. It consists in the superposition at each point of the isolated electron densities of each target atom (solved with GAMESS code [31]) located at its lattice sites, without thermal vibrations. It is an approximation to obtain bonds in a 3D electronic distribution. Fig. 1 shows a comparison of the three electron density models through a straight line in {1 1 1} direction in silicon. We can see that the IADS electron density is closer to the true bond density than the ZBL one. We do not know, at this moment, if this should be a good approximation for other materials than silicon, but we expect this will be good enough for non-polar covalent materials. The simulation results shown for compound materials below use IADS electron density and they are a good fit.

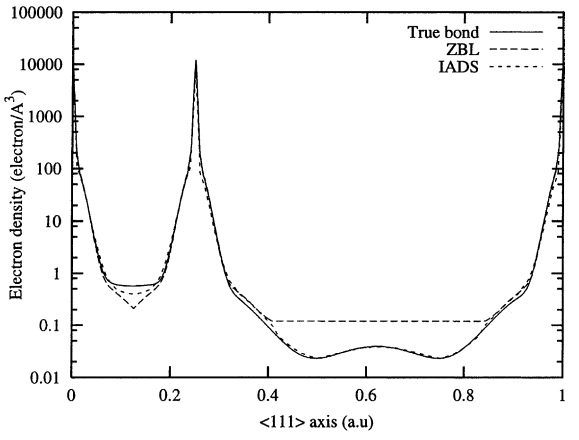

Fig. 1. Comparison between ZBL, IADS and true bond densities along {1 1 1} direction in silicon.

Simulations without free parameters [32] have also proved the necessity of using a 3D electron density distribution.

2.4. Damage accumulation

In order to deal with high dose implantations the simulator must include some damage accumulation model. It will be important especially in channelling cases.

Our damage model is based on the modified Kinchin–Pease model [1,33], and its modelization has two parts: the *defect generation/recombination* and the *damage simulation* which we will describe in the computing algorithms section.

The whole crystal is divided into 100 slices in depth. In order to work with it we define the area of the slice as $A = N_s/\Phi$ where N_s is the number of ions simulated and Φ is the dose implanted. When an ion goes out the slice it enters by the opposite side (periodicity).

2.4.1. Defect generation/recombination

The number of point defects generated, n, is proportional to the energy lost, E, by nuclear scattering in each sector:

$$n = \frac{kE}{2E_d} \quad (5)$$

where $k = 0.8$ is a constant and E_d is the displacement threshold energy.

Part of the point defects generated recombines with other defects, so the net increase of point defects after recombination, Δn, is given by:

$$\Delta n = n f_{surv}\left(1 - \frac{N}{N_\alpha}\right) \quad (6)$$

where f_{surv} is the fraction of point defects surviving both intracascade and intercascade recombination and it is adjusted for each implanted kind of projectile; N, the previous local defect density; and N_α, the local defect density necessary to reach amorphization.

3. Computing algorithms

3.1. Inelastic losses: integration methods

We have experienced that the integration schemes for the two energy loss components are very important to achieve correct results within the BCA. As a result, we use a hybrid integration method, between MD and the BCA model, in order to improve the numerical integrations.

For the non-local electronic losses the straight projectile trajectory is sampled (see Fig. 2, where a straight movement is considered for the projectile and target) having into account the potential energy at each point due to the surrounding neighbors ($E_p(x)$), the elastic energy transfer to the target ($E_T(x)$) and also the electronic losses accumulated up to this point ($S_{non\text{-}local}(x)$). The local kinetic energy for the projectile is calculated as:

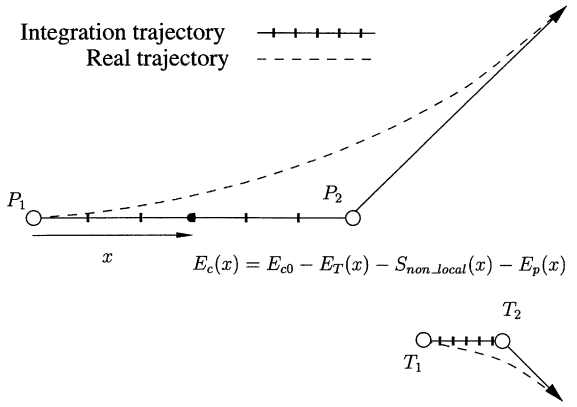

Fig. 2. Integration scheme for the non-local electronic stopping.

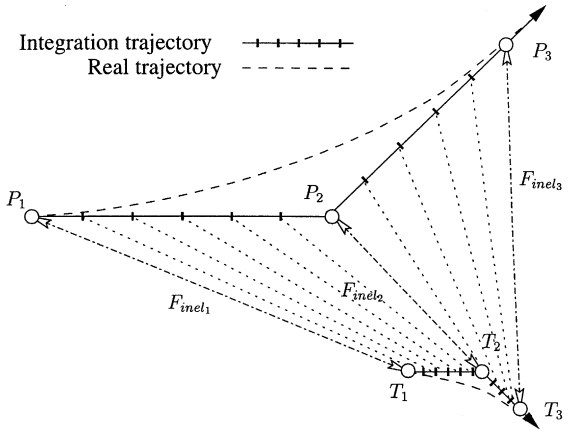

Fig. 3. Integration scheme for the local inelastic stopping.

$$E_c(x) = E_{c0} - E_T(x) - S_{\text{non-local}}(x) - E_p(x) \quad (7)$$

where E_{c0} is the initial kinetic energy at this collision. Knowing that $v = (2E_c/M_1)^{1/2}$ the non-local electronic losses are integrated as shown in Eq. (1).

The local inelastic losses are integrated along the straight incoming and outgoing trajectories (Fig. 3) of the projectile. A straight displacement is assumed for the target. At each point, the force F_{ij} between the projectile and the target is evaluated. The length of the outgoing trajectory is selected long enough to account for all the interaction. We consider the contributions of all the targets involved in the collision.

3.2. Statistical noise improvement algorithm

In order to reduce the calculation time and to improve the accuracy of the simulated profiles a 3D rare event algorithm is implemented [34].

The straightforward way to obtain a statistically significant concentration at all depths of the profile is to run many simulated cascades. Most of the ions will stop near the main peak. The majority of the computer effort will not improve the accuracy of the tail or low concentration zones.

With the atom splitting scheme [34] at certain depths, the ion is split into two *virtual* ions with half-statistical weight of unsplit ion. The virtual ions generated have the same position and velocity as the parent ion. Their final trajectories are, however, different due to the thermal vibration effects. In the end, we obtain practically the same number of virtual ions at each bin of the histogram profile improving the statistics on low concentration zones.

In the ion implant simulation there are two rare event cases of particular interest to be considered to improve the statistics:

3.2.1. Channelled ions

This case occurs when the projectile travels through a crystal channel. It looses its energy mainly by inelastic interaction without having hard nuclear (elastic) collisions. We monitor the total distance travelled by the ion to improve statistics at both the deep and the lateral regions.

We define, in a general way, a border d_i as either a depth reached by the ion or as the total distance travelled by the projectile. When the ion reaches the border with the next index, it is splitted into two virtual ions with half-statistical weight. Fig. 4 shows an example of how a real ion is splitted several times into several virtual ions when it reaches certain borders. We also show the statistical weight associated with each virtual ion.

The borders cited above are calculated by solving the following equation

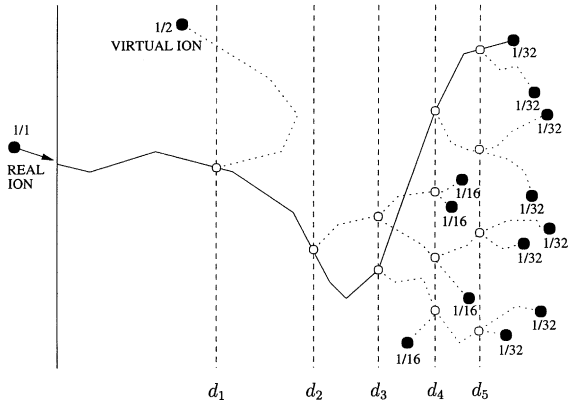

Fig. 4. Rare event algorithm with lateral or depth enhancement scheme.

$$\int_0^{d_i} C(x)\,\mathrm{d}x = (1-(1/2)^{i}) \int_0^{\infty} C(x)\,\mathrm{d}x \tag{8}$$

where $C(x)$ is the dopant histogram profile at a certain depth (or total distance travelled) x.

With this scheme we can recalculate the splitting borders dynamically in order to improve the statistics in specific regions. We do not need to know a priori the borders. First, N_0 real ions are simulated without the rare event algorithm, in order to obtain some statistics to estimate the initial borders d_i. Then, the algorithm is activated and every N_{interval} real ions the borders are recalculated. This value must be large enough (i.e. $N_{\text{interval}} = 100$) not to increase the computation time. When we have attained the desired statistical accuracy in the rare event region, the algorithm is automatically deactivated.

Fig. 5 shows the dopant profiles obtained for an implantation of boron into silicon with 2 keV, with and without the trajectory-length selection scheme. We observe the better definition of the profile tail. The simulation time is doubled with the algorithm, but the time needed to obtain the same accuracy without the algorithm would have been 10 times longer [34].

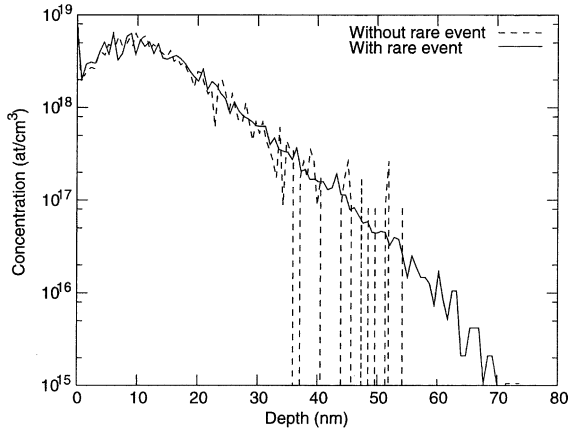

Fig. 5. Implantation of B (tilt = 7°, rotation = 30°) → Si{100}, 2 keV simulated with $N_{\text{ion}} = 2000$ real ion with and without the trajectory-length selection scheme.

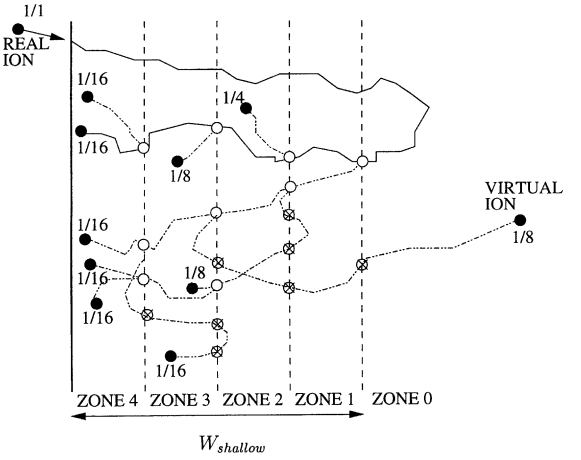

Fig. 6. Rare event algorithm with shallow region enhancement scheme.

3.2.2. Projectiles in the shallow region of the impurity profile

These ions have probably lost most of their energy in a few hard nuclear collisions at the beginning of their flight. They have relatively low energy and are near the surface.

When we simulate medium and high energy implants there is some statistical noise in the shallow region of the profiles due to the (few) ions who have lost their energy at the beginning of their travel. We use two conditions to identify these cases:

First, an energetic condition: the energy decreases below a user defined threshold energy, $E \leqslant E_{\text{th}}$, that is generally a percentage of the initial energy. Ions that verify this condition are likely to stop nearby.

Second, a positional condition: we consider the shallow region (Fig. 6) defined by

$$W_{\text{shallow}} = p_{\text{d}}(D_{\max} - D_{\min}) \tag{9}$$

where $D_{\max}$ is the maximum depth reached by an implanted ion; $D_{\min}$, the positive minimum depth of the current profile and p_{d}, the percentage of the whole profile that the user considers to be the shallow region. We divide W_{shallow} into N equal zones. Initially the projectile is considered to have index 0 ($n_{\text{index}} = 0$, with unity statistical weight). When the first condition ($E \leqslant E_{\text{th}}$) is met we compare the current depth of the projectile,

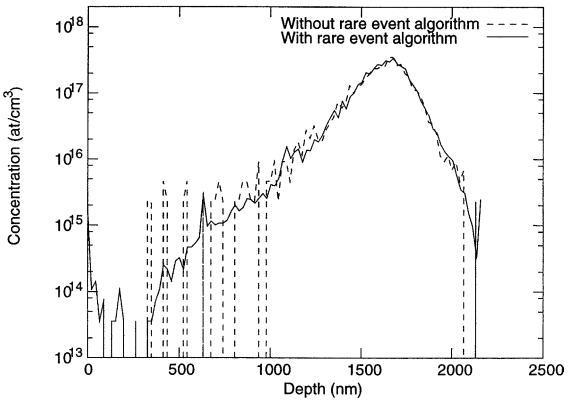

Fig. 7. Profile comparison for an implantation of B (7°, 30°) → Si{100}, 1 MeV simulated with $N_{ion} = 2000$ real ion with an without the shallow region enhancement scheme.

$D_{projectile}$ with the border that defines the next index as shown in the equation below

$$D_{projectile} < D_{min} + W_{shallow}\left(1 - \frac{n_{index}}{N}\right) \quad (10)$$

If the two conditions are met we split the current ion into two virtual half-weighted ions and we increment n_{index}, and the same procedure is applied to both virtual ions again. Finally, the algorithm is deactivated when the statistical accuracy required is reached.

Fig. 7 shows a retrograde implant profile of boron into silicon with and without the shallow region enhancement scheme. We note the better definition of that region. The simulation time is increased by 50% with respect to not using the algorithm, but the time necessary to obtain the same statistical accuracy by increasing the number of projectiles simulated (by 10), increases the time by 760% in this case [34].

3.3. Damage accumulation

Our damage model is based on the modified Kinchin–Pease model [1,33] described above, and its modelization has two parts: the defect generation/recombination and the damage simulation.

3.3.1. Defect generation/recombination

In 1D, the crystal is divided into slices perpendicular to the depth axis. Eqs. (5) and (6) are applied to each sector to calculate its defect density.

In order to reduce the computational overload generated by following the complete cascade a simplification can be used [35,33]. The simulator considers only the primary ion. When a scattering event occurs the energy transferred to the target atom E_T is compared with a cut-off energy (e.g. $E_{CutOff} = 24$ eV, for boron into silicon). If E_T is greater than the cut-off energy then the algorithm considers only a transferred energy of $E_T = E_{CutOff}$. This energy is defined as the energy needed to amorphize completely a sector as the result of a single collision. This approximation does not take into account the energy deposited by secondary atoms. The calculation time reduction using this approximation is about the 30%. The N_α and f_{surv} parameters can vary within this approximated scheme.

3.3.2. Damage simulation

The local defect density, N, is a measure of the amorphization of each sector in the crystal. If the sector is completely amorphous, a random rotation of the crystal lattice is performed for each collision as did MARLOWE [7]. For a partially amorphized section the rotation probability is N/N_α. After the collision, the original crystal orientation is restored.

3.4. Speeding-up the calculation

Several strategies have been employed throughout the code to speed-up the calculation. When possible, look-up tables [8] previously calculated are used: elastic interaction, local and non-local inelastic losses, etc. The tables are calculated and stored in disk, for future use, for each projectile–target atom combination. By doing this the computation time is not degraded compared to conventional BCA approach, while it is much more predictive and about two orders of magnitude faster than MD.

3.5. Selection of the target atoms

BCA needs a method to select the next target atoms to collide with. We begun using the MARLOWE [7] target atom selection method. It accepts target atoms that are in the direction of ion movement and have an impact parameter smaller than a given value ($p < p_{max}$) and a distance along movement direction to the point nearest the target $\xi > \xi_{min}$, where ξ_{min} was obtained from the last collision [36] to prevent successive collisions with the same target atom. We verified the identical behavior between MARLOWE and our simulator for selecting the target atoms, step by step: first we ran a MARLOWE simulation obtaining the maximum detail; then we analyzed the output file, collision by collision, comparing it with our program results for the same conditions.

We observed that, randomly, the mechanism missed a target atom or recollided with the same atom. This is due to the thermal vibrations, that displaces the target atom from its lattice position.

To avoid this wrong behavior, that mainly modifies the channelling tail, we store a list with the atoms involved in the last collision. We compare the new targets

with the old ones, and remove the repeated ones. This replaces the ξ_{min} condition and speed-up the calculation.

4. Results

In this section we compare simulated dopant profiles with experimental ones or with results from other simulators in order to validate our enhancements to the ion implant BCA simulation and to test its prediction capabilities with compound semiconductors.

4.1. Silicon target

We first test our simulator implanting in crystalline silicon because the experimental data available. Fig. 8 shows a boron into silicon implants with 35 and 80 keV (with a 15 Å SiO_2 layer) simulated with several BCA simulators: MARLOWE 14 [36], UT-MARLOWE [4]

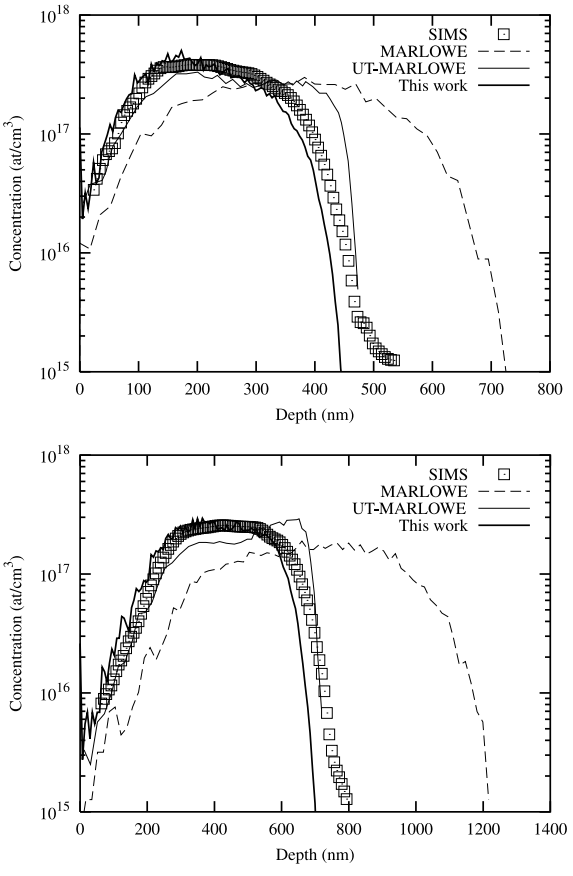

Fig. 8. Boron (0°, 0°) into {100} silicon (with a 15 Å SiO_2 layer) implant profiles with (top) 35 keV and (bottom) 80 keV. We made a comparison between SIMS profiles [4] and several BCA ion implant simulators (MARLOWE [36], UT-MARLOWE [4]) and the current work simulation results.

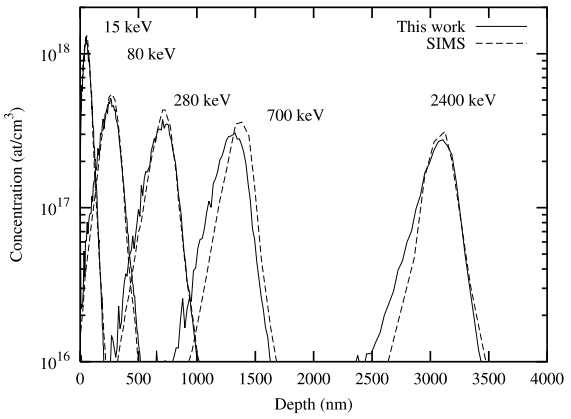

Fig. 9. Boron (7°, 30°) into {100} silicon implant (15, 80, 280, 700 and 2400 keV, with a 15 Å SiO_2 layer) comparison between SIMS profiles [4,37] and the current work simulation results.

that uses only one fitting parameter (r_s^0) and our simulator. We observe that MARLOWE penetrates much more than the experimental SIMS [4] profiles. UT-MARLOWE has the same profile range but its shape does not match with the experimental profiles. Our simulator fits better both in the range and the shape of the profile than the cited simulators.

We also compare our simulation results with SIMS experimental profiles obtained from the literature [4,21,37]. Fig. 9 represents boron implanted into silicon for several energies showing good agreement with experiments. All implants use the same $r_s^0 = 1.85$.

Fig. 10 shows implants of arsenic into silicon for several energies and implant conditions. For this ion–target combination we use $r_s^0 = 2.0$ for all conditions.

Fig. 11 shows a high dose, 8×10^{15} at/cm^2, boron into silicon implants for 15 and 80 keV and presents a

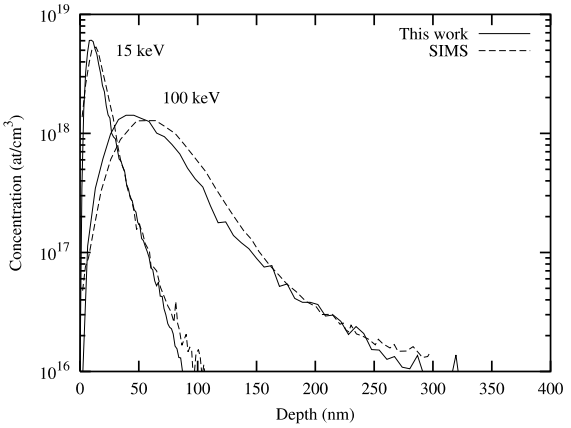

Fig. 10. Arsenic (8°, 30°) with 15 and 100 keV into {100} silicon implant comparison between SIMS profiles [21] and the current work simulation results.

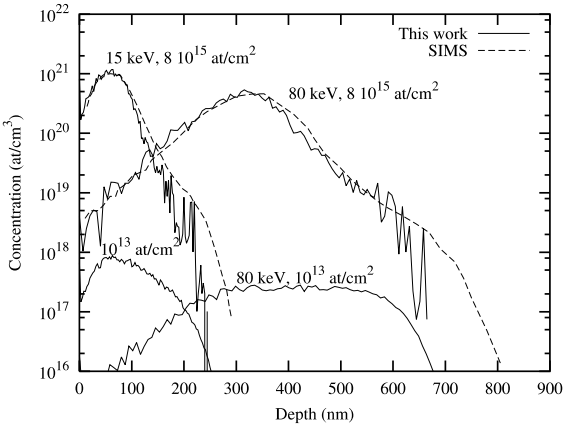

Fig. 11. High dose, 8×10^{15} at/cm^2, boron (0°, 0°) with 15 and 80 keV into {1 0 0} silicon implant comparison between SIMS profiles [37] and the current work simulation results. We note the differences with the low dose simulation results.

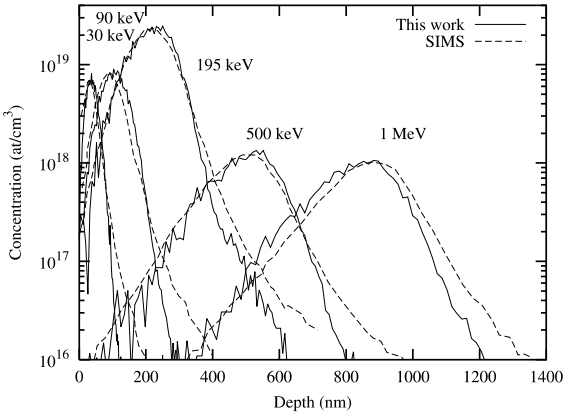

Fig. 12. Aluminum (12.5°, 30°) into 6H-SiC, 30, 90, 195, 500 and 1000 keV implants with doses of 3×10^{13}, 7.9×10^{13}, 3.8×10^{14}, 3×10^{13} and 3×10^{13} at/cm^2 respectively. The orientation of the wafer flat is {1 1 $\bar{2}$ 0} and the wafers are cut 3.5° off-axis from the {0 0 0 1} plane toward the {1 1 $\bar{2}$ 0} direction [39].

good agreement with SIMS profiles. The damage model works well here.

These examples show the prediction capabilities of the models implemented in our simulator for a wide range of implant conditions (orientation, energy, etc.) [38]. To be able to simulate a new ion species only one parameter, r_s^0 would be necessary to fit.

4.2. Silicon carbide target

In order to check the capability of the ion implant simulation in compound materials, we show some implant examples into 6H-SiC with several projectiles. Ion implantation is almost the only current method to dope silicon carbide. We used the IADS electron density approach and so we only fitted the r_s^0 parameter.

Fig. 12 shows an aluminum implant into 6H-SiC. The tilt angle is 12.5° and the rotation is 30°. The orientation of the wafer flat is {1 1 $\bar{2}$ 0} and the wafers are cut 3.5° off-axis from the {0 0 0 1} plane toward the {1 1 $\bar{2}$ 0} direction. We compare the simulation results of 30, 90, 195, 500 and 1000 keV aluminum implants with the SIMS experimental [39] profiles. A very good agreement is found. For Al into SiC we use $r_s^0 = 1.70$, which is not too different from the values used for the silicon target implants. The damage accumulation is not important for the doses simulated.

Fig. 13 represents 40, 100 and 300 keV arsenic implants into 6H-SiC with the same conditions cited above ($r_s^0 = 1.75$). Again, they match very well.

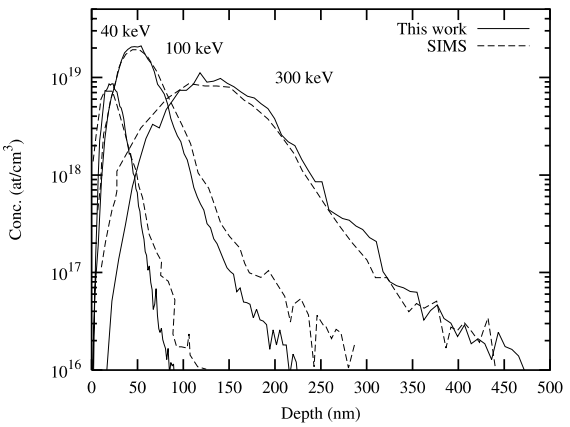

Fig. 13. Arsenic (12.5°, 30°) into 6H-SiC, 40, 100 and 300 keV implants with doses of 2×10^{13}, 9.9×10^{13} and 1.1×10^{14} at/cm^2 respectively. The orientation of the wafer flat is {1 1 $\bar{2}$ 0} and the wafers are cut 3.5° off-axis from the {0 0 0 1} plane toward the {1 1 $\bar{2}$ 0} direction [39].

4.3. Gallium arsenide target

Special characteristics for this material are a very low Debye temperature (360 K) and its softness. The damage accumulation will be important even for low doses. We fitted $N_\alpha = 6 \times 10^{20}$ at/cm^3 and $f_{surv} = 0.09$.

Fig. 14 shows silicon into GaAs (REO: random equivalent orientation) and {1 0 0} channel, $r_s^0 = 2.0$) implants at 150 keV, 3×10^{13} at/cm^2 compared with SIMS profiles [40]. We note that even for different orientations the agreement is good.

As shown in Fig. 15 we must only fit the r_s^0 when we change the projectile. It shows a comparison between selenium into GaAs (REO and {1 0 0} channel, $r_s^0 = 1.7$)

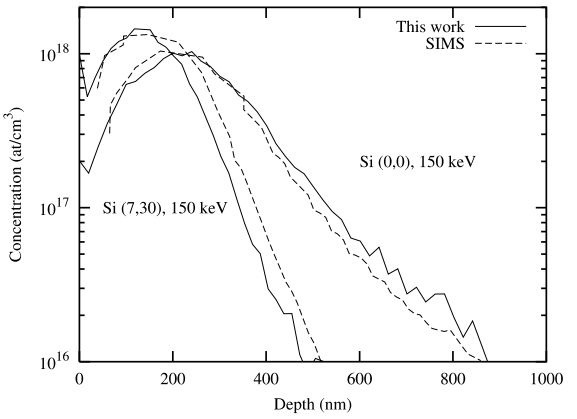

Fig. 14. Silicon (REO and {100} channel) implanted [40] into GaAs at 150 keV.

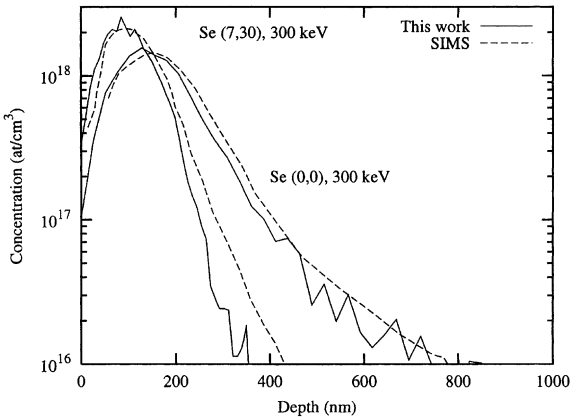

Fig. 15. Selenium (REO and {100} channel) implanted [40] into GaAs at 300 keV.

implants at 300 keV, 3×10^{13} at/cm^2, and SIMS profiles [40].

5. Conclusions

A new BCA ion implant simulator is reported. It gather some of the best physical models and simulation algorithms, including a novel hybrid integration scheme for the inelastic energy losses. It also uses ab initio physical description of the electron distribution for the target atoms. For low implant doses, the simulator is capable of predicting the impurity implant profiles of a wide range of projectile atoms and for different target materials with only one adjustable parameter (r_s^0) for each projectile–target material combination. For high doses, there are two additional parameters (f_{surv}, N_α) to fit. Also several strategies have been used in order to achieve a very fast ion implant simulator.

Acknowledgements

This work was performed under the auspices of the Junta de Castilla y León (VA 14/00B) and the DGICYT project no. PB 98-0398.

References

[1] Klein KM, Park C, Tasch AF. IEEE Trans Elect Dev 1992;39(7):1614–21.
[2] Posselt M. Rad Eff Def Sol 1994;130–131:87.
[3] Murthy CS, Srinivasan GR. IEEE Trans Elect Dev 1992; 39(2):264–73.
[4] Cai D, Gronbech-Jensen N, Snell CM, Beardmore KM. Phys Rev B 1996;54(23):17147–57.
[5] International Technology Roadmap for Semiconductors. Semiconductor Industry Association; 1999.
[6] Ziegler JF, Biersack JP, Littmark U. The stopping and range of ions in solids. New York: Pergamon Press; 1985.
[7] Robinson MT, Torrens IM. Phys Rev B 1974;9(12):5008–24.
[8] Arias J, Jaraiz M, Pelaz L, Bailón L, Barbolla J. Nucl Instr Meth B 1995;102:228–31.
[9] Arias J, Jaraiz M, Rubio JE, Pelaz L, Marqués LA, Barbolla J. J Mater Sci Tech 1995;11:1191–3.
[10] Arias J, Hernández J, Jaraiz M, Bailón L, Barbolla J. Conferencia de Dispositivos Electrónicos. Barcelona, 1997.
[11] Beardmore KM, Gronbech-Jensen N. Phys Rev E 1998;57(6):7278–87.
[12] Buschhorn G, Diedrich E, Kufner W, Rzepka M, Genz H, Hoffmann-Stascheck P, et al. Phys Rev B 1997;55(10): 6196–202.
[13] Charles K. Reverté, Barcelona, 1993.
[14] Hou M, Robinson MT. Nucl Instr Meth 1976;132:641–5.
[15] Marion JB. Classical dynamics of particles and systems. New York: Academic Press, Inc.; 1986.
[16] DMol is a trademark of Bio Sym Inc., San Diego, CA, 2000.
[17] Hernández J. PhD thesis. Valladolid, Spain: University of Valladolid; 2000.
[18] Hernández J, Jaraiz M, Arias J, Bailón L, Barbolla J, Rubio A, et al. Conferencia de Dispositivos Electrónicos. Madrid: 1999.
[19] Hernández J, Jaraiz M, Arias J, Barbolla J, Bailón L, Rubio A. Mat. Res. Soc. Symp. San Francisco: 1998.
[20] Brandt W, Kitagawa M. Phys Rev B 1982;25(9):5631–7.
[21] Cai D, Snell CM, Beardmore KM, Gronbech-Jensen N. Int J Modern Phys C 1998;9(3):459–70.
[22] Echenique PM, Nieminen RM, Ritchie RH. Solid State Commun 1981;37:779–81.
[23] Bethe HA. Ann Phys (NY) 1930;5:325.
[24] Rubio A. Dpto. Física Teórica, Facultad de Ciencias, Univ. de Valladolid, 1997, private communication.
[25] Kishinevskii LM. Bull Acad Sci USSR, Phys Ser 1962; 26:11433.
[26] Firsov OB. Sov Phys JETP 1959;36:1076–80.

[27] Morris S, Lin D, Yang SH, Tian S, Parab K, Tasch AF. Mat Res Soc Symp. 1996.
[28] Dort MJ, Woerlee PH, Walker AJ. Solid State Electron 1994;37(3):411–4.
[29] Klein KM, Park C, Tasch AF. Nucl Instr Meth B 1991;59/60:60–4.
[30] Posselt M, Schmidt B, Feudel T, Strecker N. Mater Sci Eng B 2000;71:128–36.
[31] Schmidt MW, Baldridge KK, Boatz JA, Elbert ST, Gordon MS, Jensen JJ, et al. J Comput Chem 1993;14:1347–63.
[32] Sillampäa J, Nordlund K, Keinonen J. Phys Rev B 2000;62(5):3109–16.
[33] Kinchin GH, Pease RS. Rep Progr Phys 1955;18:1–51.
[34] Hernández-Mangas JM, Arias J, Jaraíz M, Bailón L, Barbolla J. Nucl Instr Meth B 2001;174:433–8.
[35] Wang G, Tian S, Morris M, Obradovich B, Balamurugan G, Tasch A. Microelectronic Device Technology, Austin TX, USA, SPIE-Int, Soc Opt Eng, 1997. p. 324–33.
[36] Robinson MT. Phys Rev B 1989;40(16):10717–26.
[37] Texas University of Austin. UT-MARLOWE 5.0 User's guide. 1999. http://homer.mer.utexas.edu/TCAD/utmarlowe.
[38] Hernández-Mangas JM, Arias J, Jaraíz M, Bailón L, Barbolla J. J Appl Phys, submitted for publication.
[39] Ahmed S, Barbero CJ, Sigmon TW, Erickson JW. J Appl Phys 1995;77(12):6194–200.
[40] Wilson RG, Deline VR. Appl Phys Lett 1980;37(9):793–6.